

Numerical and Experimental Investigation of the Flow around a three-dimensional SD7003 Wing

Eike Tangermann, Markus Klein

Numerical Methods in Aerospace Engineering
 Universität der Bundeswehr München
 85577 Neubiberg, Germany
 eike.tangermann@unibw.de,
 markus.klein@unibw.de

Sebastian L. Herbst, Rainer Hain, Christian J. Kähler

Institute of Fluid Mechanics and Aerodynamics
 Universität der Bundeswehr München
 85577 Neubiberg, Germany
 sebastian.herbst@unibw.de, rainer.hain@unibw.de,
 christian.kaehler@unibw.de

ABSTRACT

The simulation of laminar separation is a challenge for turbulence models in computational fluid dynamics. Most previous investigations have focused on quasi two-dimensional configurations with airfoil sections. In the present investigation the geometry is extended to a fully three-dimensional wing introducing 3D effects like tip vortices to the separation and transition process. This setup has been investigated both by experiments and by computational simulation with the experimental view by PIV measurements in the central plane and CFD with turbulence-resolving hybrid methods. Despite the complexity of the case good agreement of experimental and numerical results can be achieved for some cases, while for one case the turbulence model is not capable of reproducing the separation process. Further it will be shown, that common simplifications of the geometry appear to have a significant influence on the flow reproduction in this setup.

INTRODUCTION

Laminar flow separation followed by transition to turbulence is a key feature in external aerodynamics. Its correct prediction is a major challenge for turbulence models in computational fluid dynamics. A common configuration to investigate this process is the SD7003 airfoil from the Selig and Donovan airfoil series (Selig *et al.* (1989)). Its characteristics with respect to laminar flow separation are well-known and have been investigated in numerous previous studies both experimentally and numerically. Typically for the quasi two-dimensional airfoil configuration at Reynolds numbers lower than 10^5 the laminar flow separation can be observed already at an angle of attack below 4° in sufficiently laminar conditions of the approaching flow. In the shear layer on top of the separation bubble Kelvin-Helmholtz instability arises and triggers the transition to turbulent flow. The plane Kelvin-Helmholtz vortices transform into three-dimensional turbulence, which leads to reattachment of the flow to the surface by increased transport of momentum.

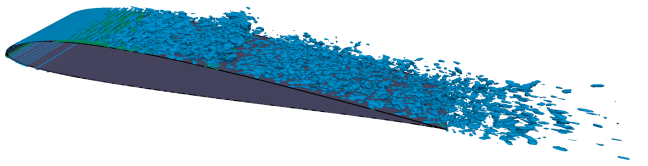


Figure 1. DNS of flow over quasi two-dimensional SD7003 airfoil configuration.

Experiments of the setup have been carried out in several facilities featuring wind tunnels, water tunnels and tow tanks (Ol *et al.*

(2005)). Most available experimental investigations of the separation process apply particle image velocimetry to identify the separation region and features of the flow over the airfoil (Hain *et al.* (2009); Burgmann *et al.* (2008)).

The SD7003 airfoil also has been investigated using numerical simulation methods. Common RANS models typically fail to produce the correct behavior of separation and transition. However, with models adapted for this specific case good agreement with validation data can be achieved (Catalano & Tognaccini (2011b); Windt *et al.* (2006)). To predict the process in a more universal approach, turbulence resolving methods need to be applied. Only few solutions from DNS are available (Carton de Wiart & Hillewaert (2012)), since the method requires high computational effort. Several authors have presented solutions with various LES methods like Catalano & Tognaccini (2011a) and Galbraith & Visbal (2009), which show a certain range of solutions depending on the turbulence model applied and on the width of the resolved domain in spanwise, periodic direction. Finally, hybrid models also are capable of reproducing the process of separation and transition as shown by Tangermann & Klein (2016) for the standard SA-DDES model as well as by Schmidt & Breuer (2017) using a more sophisticated approach, which considers the laminar nature of the flow before the separation.

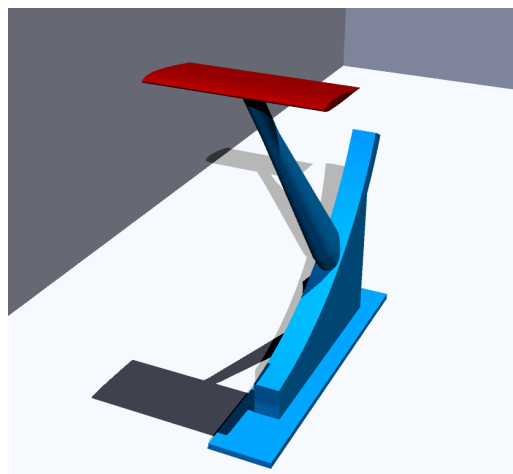


Figure 2. Wind tunnel configuration of the wing and sting.

In the present study a fully three-dimensional wing configuration instead of the common quasi two-dimensional case is investigated with respect to laminar separation both by wind tunnel experiment as well as by computational simulation. The configuration features

a three-dimensional wing based on the SD7003 airfoil. The wing is rectangular with an aspect ratio of two. For the measurements in the wind tunnel the wing is mounted on a sting, which is attached on the lower side of the wing, allowing to adjust the angle of attack between -10° and 20° . Figure 2 shows the configuration with the wing colored red and the sting colored blue surrounded by wind tunnel walls. For the CFD simulations two models of the configuration have been used. Both feature the wing and the wind tunnel walls as boundary of the domain. In the first model the sting is included while in the second one only the wing is present but not the sting in order to determine the influence of the sting geometry on the flow around the wing. The Reynolds number based on the freestream velocity and the chord length is $Re = 60,000$, which would lead to a laminar separation at relatively low angles of attack in the quasi two-dimensional airfoil case.

EXPERIMENTAL SETUP

The experiments have been performed in the atmospheric wind tunnel Munich (AWM). This open circuit, suction type wind tunnel features a 22m long test section with a cross section of $1.85\text{m} \times 1.85\text{m}$. Velocities of up to 45 m/s can be achieved, though the pitch angle of the fan was optimized for the velocity of 5m/s in order to achieve stable flow conditions at low Reynolds numbers. For the characterization of the inflow conditions, streamwise turbulence intensity was measured by means of a single hot wire probe (Dantec 55P15) to $Ti_u = 0.49\%$. The velocity was measured to 4.7m/s which results in a chord Reynolds number of $Re_c = 63,000$. The wing with the selected SD7003 profile has a span of 0.4m and a chord length of 0.2m. To gain a very light model for the force and torque measurements, it is constructed of carbon fiber reinforced polymer. Forces and torques are recorded by a six component balance (ATI Nano 17) located between the sting and the wing. To determine the velocity field on the suction side, PIV measurements (2D2C) have been performed. Tracer particles of di-ethyl-hexyl-sebacat (DEHS) droplets with a diameter of approximately $1\ \mu\text{m}$ are used to visualize the flow. The measurement plane is located along the centerline of the wing and is illuminated by means of a double pulse Nd:YAG laser. In order to increase the image resolution two Imager sCMOS cameras are used in a configuration staggered along the wing covering the whole upper side as shown in Figure 3. Details are given in Table 1.

NUMERICAL SETUP

In the simulations both the complete wind tunnel configuration featuring the sting and walls has been considered as well as a free flying wing within the wind tunnel walls without the sting. This allows not only to achieve full access to the flow field but also to

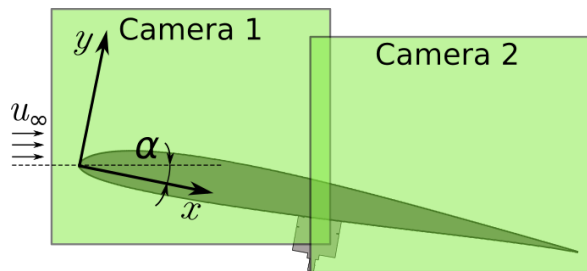


Figure 3. PIV camera setup

Parameter	
Light sheet thickness, mm	2
Sensor resolution, px	2560 x 2160
Field of view (combined), mm ²	224 x 102
Δt , μs	75
Number of images	5000
Interrogation window, px	16
Overlap, %	50
Magnification mm/px	0.048
Vector distance, mm	0.384

determine the influence of the sting construction on the actual flow around the wing.

The chord length of the wing again is $c = 0.2\text{m}$. Like in the actual wind tunnel the test section spans $9.25c \times 9.25c$. A domain length of $31c$ is considered, extending $15c$ upstream and downstream of the wing, respectively. To reduce the computational effort only the wing and the upper part of the sting are viscous walls with fully resolved boundary layer fulfilling $y^+ < 1$ for the first cell. All remaining walls including the lower part of the sting are free-slip boundaries and do not feature a boundary layer.

The geometrical configuration requires to generate a new mesh for each angle of attack to be investigated. The meshes are unstructured hybrid meshes with prism cells in the boundary layer region. Figure 4 gives an impression of the mesh topology. The sizes of the meshes for the different cases are listed in Table 2.

α	Sting	Number of cells
4°	no	$35 \cdot 10^6$
8°	no	$37 \cdot 10^6$
8°	yes	$42.7 \cdot 10^6$

The simulations have been performed using the OpenFOAM[®] flow solver. The case features a low velocity thus the flow can be considered incompressible. Pressure and velocity are coupled in a combined PISO and SIMPLE approach. The discretization is of second order both in space and time. The time stepping scheme is

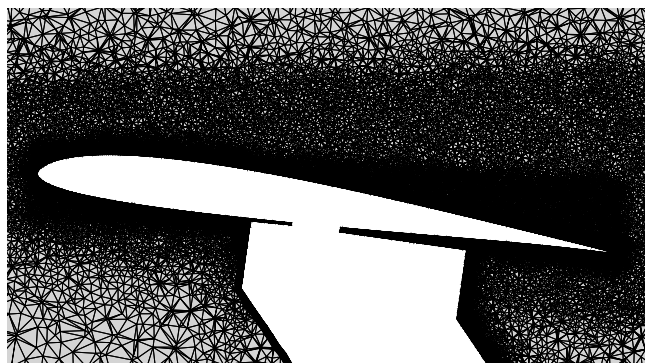


Figure 4. Central plane of the unstructured mesh around the wing for $\alpha = 8^\circ$ with sting.

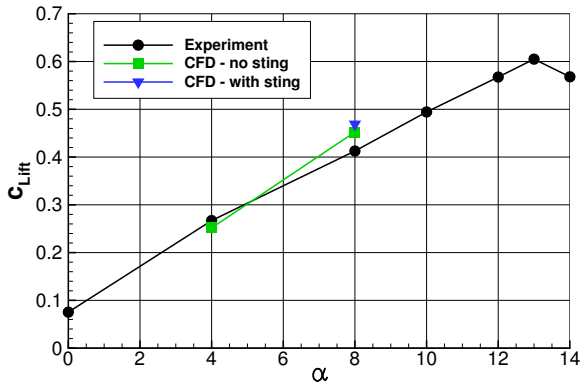


Figure 5. Lift coefficients from experiment and simulation for different angles of attack.

an implicit backward scheme, which considers one previous time step. All spatial terms are discretized with central schemes. The turbulence model is a Spalart-Allmaras based DDES model according to Spalart *et al.* (2006). The model blends between the SA one-equation model in RANS mode and a formulation similar to the Smagorinsky model in LES mode. The capability of this model with respect to laminar separation has been shown by Tangermann & Klein (2016) for the SD7003 airfoil, where good agreement between SA-DDES and LES calculations has been achieved. The transition to turbulent flow takes place in the shear layer, where the LES mode of the model is active, and then is transported into the boundary layer, where the model is in RANS mode.

RESULTS AND DISCUSSION

The comparison of the lift coefficient offers a first impression of the flow to be expected. The lift increases nearly linear up to an angle of attack of $\alpha = 13^\circ$ before it decreases due to the fully separated flow.

The lift produced by the simulation agrees well with the experimentally determined values. For $\alpha = 8^\circ$ the two configurations with and without a sting predict almost the same lift.

However, a closer look at the flow field reveals, that for $\alpha = 4^\circ$ the simulation does not produce a separation at all, while this can be observed in the experiment. Figure 6 shows the mean streamwise velocity in the central plane of the wing from the simulation. The flow remains attached along the whole wing. From the experiment Figure 7 shows a clear separation of the flow at $x/c = 0.286$ and it becomes attached again at $x/c = 0.783$. The transition takes place at $x/c = 0.572$, for which the criterion of $-\langle u'v' \rangle / U_0^2 > 0.001$ according to Ol *et al.* (2005) has been taken.

It is suspected, that the turbulence model prevents the flow from separating in the simulation. The separation should take place relatively far downstream, where the RANS mode of the model already has become active, thus preventing the separation.

When increasing the angle of attack to 8° the simulation also produces flow separation. This can be seen for both variants with and without the sting included in the model. However, the flow solution shows significant differences between the two cases.

The flow simulation allows to investigate the flow in its fully three-dimensional nature. Figure 8 gives an impression of the structure of the flow showing isosurfaces of Q-criterion and the separation region. In the central region of the wing it is similar to the quasi two-dimensional case. Towards the wing tip the three-dimensional nature of the flow becomes obvious. The instantaneous images

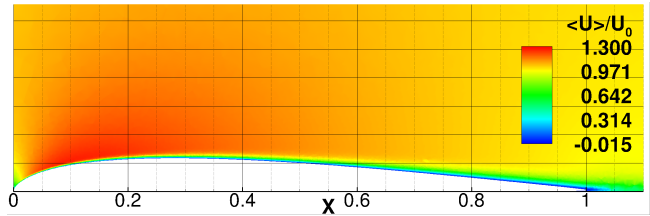


Figure 6. Velocity field from simulation, $\alpha = 4^\circ$, no sting: mean streamwise velocity $\langle u \rangle$ without separation.

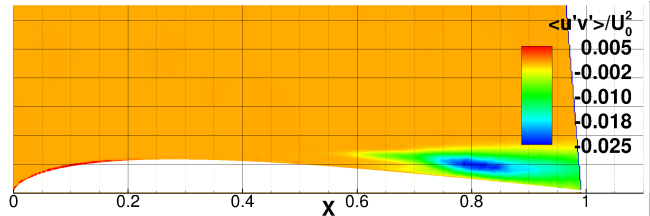
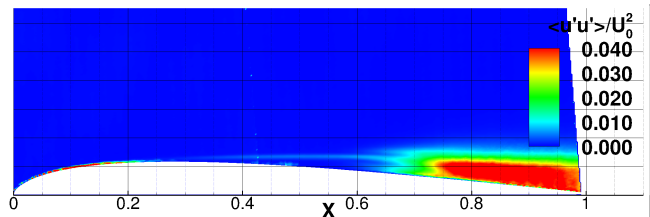
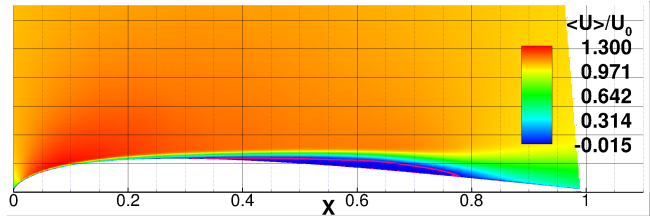


Figure 7. Velocity field from experiment, $\alpha = 4^\circ$: mean streamwise velocity $\langle u \rangle$ (top), streamwise velocity fluctuation $\langle u'u' \rangle$ (center), fluctuation cross correlation $\langle u'v' \rangle$ (bottom)

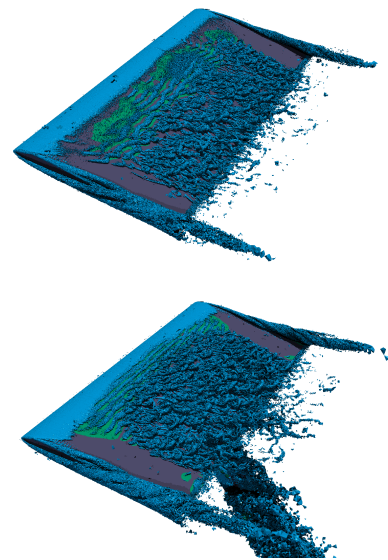


Figure 8. Three-dimensional structure of the flow. $\alpha = 8^\circ$, no sting (top) and with sting (bottom). Instantaneous Q isosurface (blue) and separation region (green).

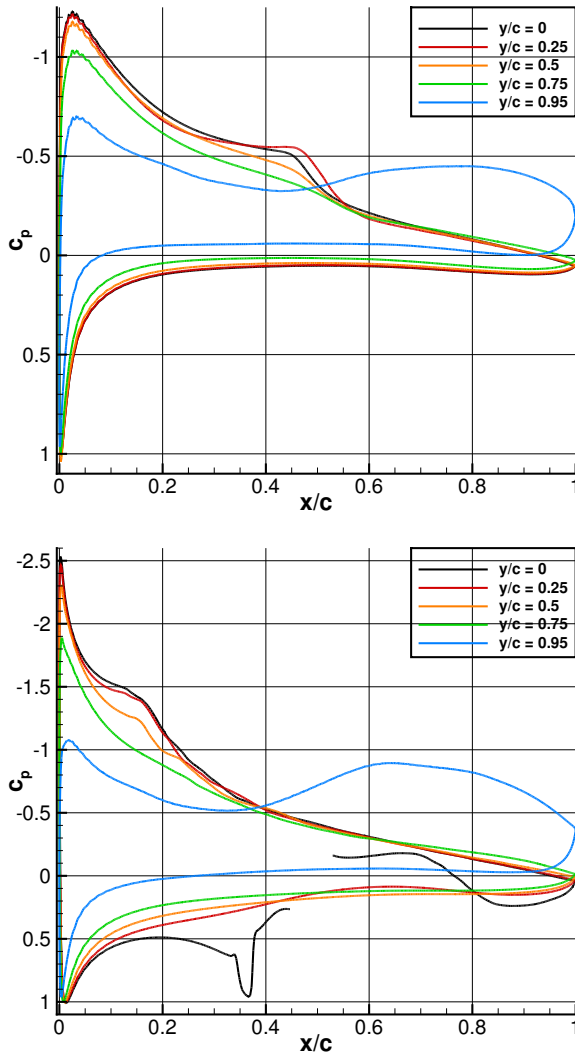


Figure 9. Pressure coefficient profile for different spanwise locations from simulation, $\alpha = 8^\circ$, no sting (top) and with sting (bottom).

show, how the wing tip vortices prevent the flow from separating by inducing velocity towards the upper side of the wing. It also shows, that the tip vortex suppresses turbulence on the upper side of the wing, the turbulent vortices identified by the Q surface are far weaker in this region.

Also a qualitative impression of the sting influence on the flow appears, when comparing the two cases. With the sting present, the flow seems to approach the wing at a higher angle of attack, which leads to a separation further upstream and a quicker transition to turbulent flow. However, the treatment of the sting with a free-slip boundary condition in its lower part introduces further uncertainty to the numerical model. Further investigation is necessary, whether the increase of the angle of attack might be caused by this specific setup and could be prevented by explicit treatment in the turbulence model or if it is a physical consequence of the sting presence.

The three-dimensional effect can also be identified in the plots of pressure coefficient from different spanwise locations in Figure 9 and those of friction coefficient in Figure 10. On the upper side for both configurations only few deviations occur between the central plane until half the span regarding pressure and surface friction. At 75% span the characteristic of the curve becomes different because the reattachment already is influenced by the tip vortex. Here the reattachment is delayed and in contrast to the inner region

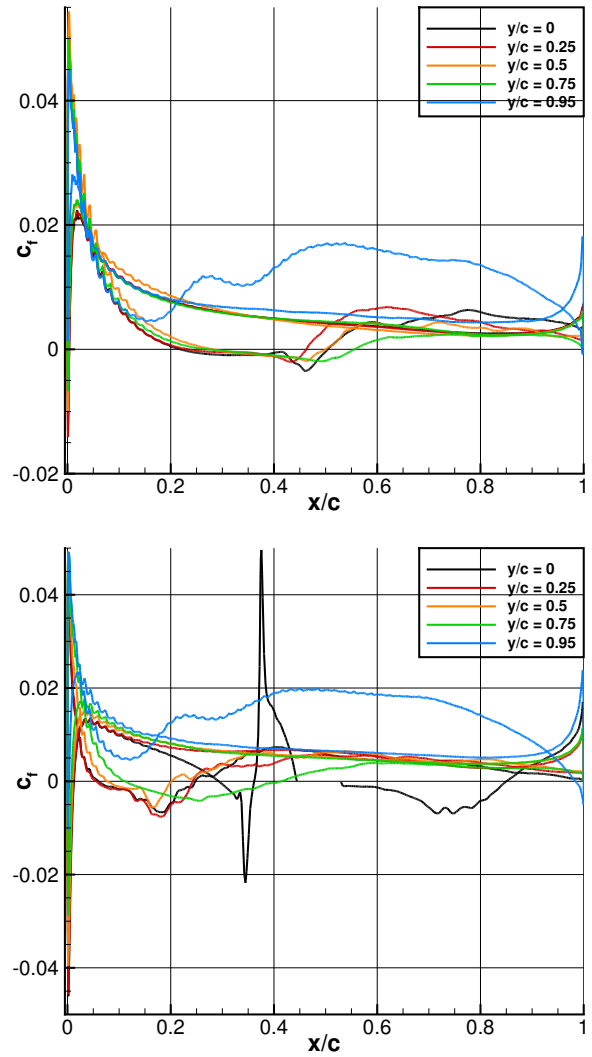


Figure 10. Friction coefficient profile for different spanwise locations from simulation, $\alpha = 8^\circ$, no sting (top) and with sting (bottom).

not introduced by a peak in the friction coefficient. At 95% span no separation occurs and the pressure distribution is dominated by wing tip effects.

On the lower side the influence of the sting occurs clearly on the centerline showing a separation before and behind it. For the other locations the direct sting influence vanishes.

Since the experimental investigation was limited to the central plane of the wing, the following evaluation will be based only on data from this location. However, as indicated by the results before this is expected to be valid within the whole inner section of the wing.

The locations of separation, transition and reattachment are summarized in Table 3 for the experiment and the two simulations at $\alpha = 8^\circ$. As indicated by the profiles of surface friction the results between the two simulations deviate significantly. While for both the experiment and the simulation featuring the sting the separation takes place at a similar location, it occurs further downstream for the simulation without the sting.

The transition again is detected by a threshold of cross correlation Reynolds stresses $\langle u'v' \rangle$ according to Ol *et al.* (2005). The simulation with sting predicts the onset of turbulence slightly upstream of the location extracted from experimental data. The experiment

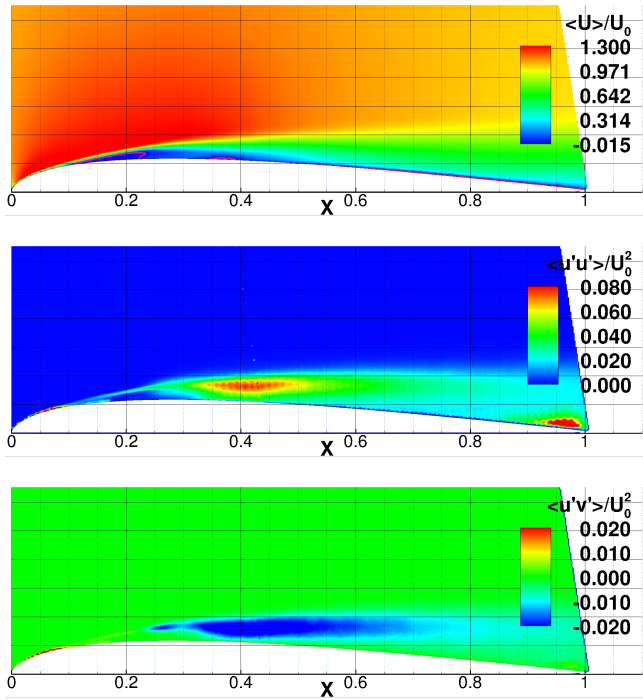


Figure 11. Velocity field from experiment, $\alpha = 8^\circ$: mean streamwise velocity $\langle u \rangle$ (top), streamwise velocity fluctuation $\langle u'u' \rangle$ (center), fluctuation cross correlation $\langle u'v' \rangle$ (bottom)

shows the reattachment downstream compared to the simulation with sting, while in the simulation without sting it takes longer to develop the re-attached flow. Without the sting in the simulation the separation does not only take place further downstream, it then also needs longer to become turbulent. After the transition the distance to reattachment is predicted similar by both simulations. Figures 11, 12 and 13 show the mean velocity and fluctuation fields in the central plane. In the contour plots of mean velocity the differences in the separation zone become obvious. The separation region detected from the experiment is thicker than those produced by the simulations. As stated before the flow becomes re-attached very soon after transition in the experiment. In the velocity contours it can be seen, that the separation region ends very suddenly. The velocity along the wing surface first remains relatively low until finally momentum is transported towards the surface by increasing turbulence. This is supported by the maximum of fluctuation intensity, which forms downstream of the reattachment. The simulation with sting also produces a maximum of turbulence shortly after reattachment. However, the level of turbulence is predicted significantly higher and the production of resolved fluctuations starts further upstream than in the experiment, which then leads to the sooner detection by the $\langle u'v' \rangle$ criterion shown in Table 3. The higher fluctuation intensity then leads to a thinner

Table 3. Separation, transition and reattachment locations (x/c) for $\alpha = 8^\circ$ on central plane. Transition detected by $-\langle u'v' \rangle / U_0^2 > 0.001$.

	separation	transition	reattachment
Experiment	0.101	0.214	0.393
CFD with sting	0.062	0.163	0.247
CFD no sting	0.219	0.404	0.504

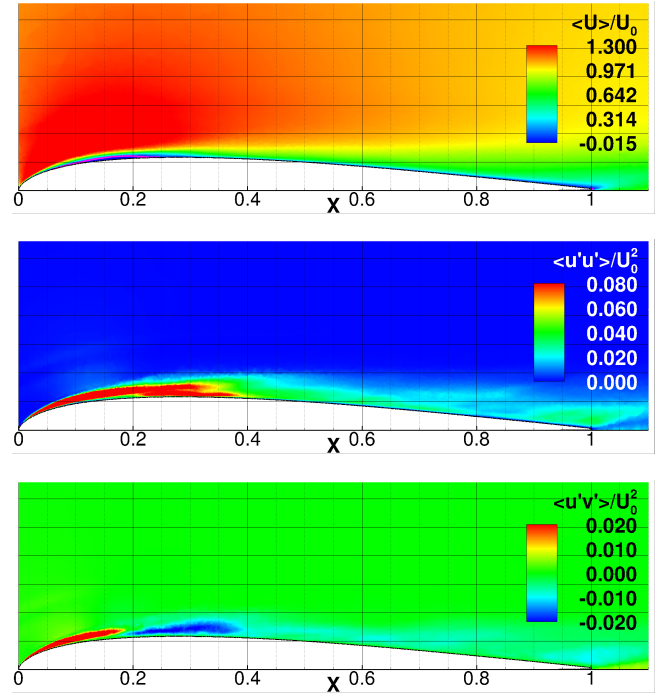


Figure 12. Velocity field from simulation, $\alpha = 8^\circ$ with sting: mean streamwise velocity $\langle u \rangle$ (top), streamwise velocity fluctuation $\langle u'u' \rangle$ (center), fluctuation cross correlation $\langle u'v' \rangle$ (bottom)

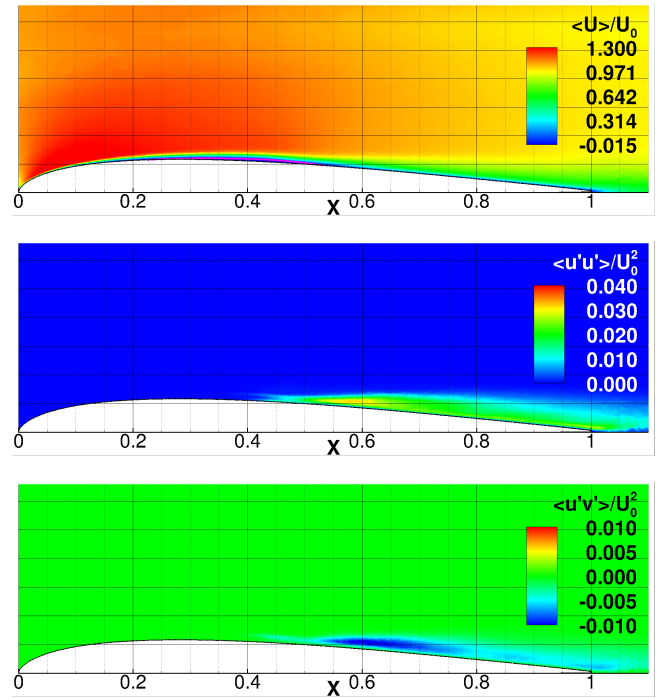


Figure 13. Velocity field from simulation, $\alpha = 8^\circ$ no sting: mean streamwise velocity $\langle u \rangle$ (top), streamwise velocity fluctuation $\langle u'u' \rangle$ (center), fluctuation cross correlation $\langle u'v' \rangle$ (bottom)

separation zone and to a faster recovery of the boundary layer. The case without sting does not only show a delayed separation, the intensity of fluctuations also stays significantly lower than in

the other case. This leads to a longer separation region but it is still produced thinner than it is seen in the experiment.

When looking at the $\langle u'u' \rangle$ fluctuations close to the trailing edge a slight influence of the sting to the upper side appears. The experiment as well as the simulation with the sting show a local increase of fluctuations, which does not occur in the simulation without sting. As seen in the plots of surface pressure and friction the flow separates behind the sting. This is a heavily unsteady process on the lower side of the wing and slightly influences the flow on the upper side by introducing pressure fluctuations around the trailing edge.

CONCLUSIONS

Experimental results of laminar separation on a three-dimensional wing have been presented together with detached eddy simulations. The simulations allow to observe the three-dimensional structure of the flow as well as the influence of the sting, which is attached in the experiment to support the wing.

The simulation at a higher angle of attack featuring the sting geometry agrees well with the experimental data concerning overall lift coefficient as well as separation location. Significant differences appear in the thickness and shape of the separation region and the turbulence intensity downstream of the separation. These phenomena as well as the lack of flow separation in the simulation of the lower angle of attack are expected to be connected with the turbulence model, which had been validated for a quasi two-dimensional setup in previous work. In this far more complex fully three-dimensional case basic reproduction of flow features still appears to be possible with this model. However, reproducing the flow in more detail or predicting the onset of separation at low angles of attack challenges the turbulence model. Thus future work will concentrate on the extension of the turbulence model.

ACKNOWLEDGEMENT

The experimental investigation has been supported by the German Research Foundation (DFG) within the project HA 6926/2-1.

REFERENCES

- Burgmann, S., Dannemann, J. & Schröder, W. 2008 Time-resolved and volumetric PIV measurements of a transitional separation bubble on an SD7003 airfoil. *Experiments in fluids* **44** (4), 609–622.
- Catalano, P. & Tognaccini, R. 2011a Large eddy simulations of the flow around the SD7003 airfoil. In *AIMETA Conference*.
- Catalano, P. & Tognaccini, R. 2011b RANS analysis of the low-Reynolds number flow around the SD7003 airfoil. *Aerospace Science and Technology* **15** (8), 615–626.
- Galbraith, M. & Visbal, M. 2009 *Implicit large eddy simulation of low-Reynolds-number transitional flow past the SD7003 airfoil*. University of Cincinnati.
- Hain, R., Kähler, C. J. & Radespiel, R. 2009 Dynamics of laminar separation bubbles at low-Reynolds-number aerofoils. *Journal of Fluid Mechanics* **630**, 129–153.
- Ol, M., McCauliffe, B., Hanff, E., Scholz, U. & Kaehler, C. J. 2005 Comparison of laminar separation bubble measurements on a low Reynolds number airfoil in three facilities. In *35th AIAA fluid dynamics conference and exhibit*, p. 5149.
- Schmidt, S. & Breuer, M. 2017 Source term based synthetic turbulence inflow generator for eddy-resolving predictions of an airfoil flow including a laminar separation bubble. *Computers & Fluids* **146**, 1–22.
- Selig, M. S., Donovan, J. F. & Fraser, D. B. 1989 *Airfoils at low speeds*. HA Stokely.
- Spalart, P. R., Deck, S., Shur, M. L., Squires, K. D., Strelets, M. Kh. & Travin, A. 2006 A New Version of Detached-eddy Simulation, Resistant to Ambiguous Grid Densities. *Theoretical and Computational Fluid Dynamics* **20** (3), 181–195.
- Tangermann, E. & Klein, M. 2016 LES and DES of Laminar Separation on an SD7003 Airfoil. In *6th Symposium on hybrid RANS-LES Methods*.
- Carton de Wiart, C. & Hillewaert, K. 2012 DNS and ILES of transitional flows around a SD7003 using a high order discontinuous Galerkin method. In *Seventh international conference on computational fluid dynamics (ICCFD7), Big Island, Hawaii*.
- Windte, J., Scholz, U. & Radespiel, R. 2006 Validation of the RANS-simulation of laminar separation bubbles on airfoils. *Aerospace science and technology* **10** (6), 484–494.